Nanoscale

Light and Complex 3D MoS2/graphene Heterostructures as an Efficient Catalyst for the Hydrogen Evolution Reaction

Journal:	*Nanoscale*
Manuscript ID	NR-ART-11-2019-009564.R1
Article Type:	Paper
Date Submitted by the Author:	18-Dec-2019

Complete List of Authors:	Teich, Jonah; Tel Aviv University, Materials Science and Engineering Dvir, Ravit; Tel Aviv University, Materials Science and Engineering Henning, Alexander; Northwestern University, Materials Science and Engineering Hamo, Eliran; Tel Aviv University, Materials Science and Engineering Moody, Michael; Northwestern University, Materials Science and Engineering Jurca, Titel; Northwestern University, Chemistry Cohen, Hagai; Weizmann Institute of Science, Chemical Research Support Marks, Tobin; Northwestern University, Chemistry Rosen, Brian; Tel Aviv University, Materials Science and Engineering Lauhon, Lincoln; Northwestern University Ismach, Ariel; Tel Aviv University, Materials Science and Engineering

SCHOLARONE™
Manuscripts

Light and Complex 3D MoS_2/Graphene Heterostructures as an Efficient Catalyst for the Hydrogen Evolution Reaction

Jonah Teich,*† Ravit Dvir,*† Alex Henning,*§ Eliran Hamo,† Michael J. Moody,§ Titel Jurca,‡ Hagai Cohen,⊥ Tobin J. Marks,‡§ Brian A. Rosen,† Lincoln J. Lauhon§ and Ariel Ismach†#

† Department of Materials Science and Engineering, Tel Aviv University, Ramat Aviv, Tel Aviv, 6997801, Israel
§ Department of Materials Science and Engineering, Northwestern University, Evanston, IL 60208, United States
‡ Department of Chemistry, Northwestern University, Evanston, IL 60208, United States
⊥ Weizmann Inst Science, Department of Chemical Research Support, IL-76100 Rehovot, Israel
* These authors contributed equally to this work
# E-mail: aismach@tauex.tau.ac.il

ABSTRACT

Multi-component 3D porous structures are highly promising hierarchical materials for numerous applications. Herein we show that atomic-layer deposition (ALD) of MoS_2 on graphene foams with variable pore size is a promising methodology to prepare complex 3D heterostructures to be used as electrocatalysts for the hydrogen evolution reaction (HER). The effect of MoS_2 crystallinity is studied and a trade-off between the high density of defects naturally presented in amorphous MoS_2 coatings and the highly crystalline phase obtained after annealing at 800 °C is established. Specifically, an optimal annealing at 500 °C is shown to yield improved catalytic performance with an overpotential of 180 mV, a low Tafel slope of 47 mV/dec, and a high exchange current of 17 $\mu A/cm^2$. The ALD deposition is highly conformal, and thus advantageous when coating 3D porous structures with small pore sizes, as required for real-world applications. This approach is enabled by conformal thin film deposition on porous structures with controlled crystallinity by tuning the annealing temperature. The results presented here therefore serve as an effective and general platform for the design of chemically and structurally tunable, binder-free, complex, lightweight, and highly efficient 3D porous heterostructures to be used for catalysis, energy storage, composite materials, sensors, water treatment, and more.

INTRODUCTION

The large ecological footprint of fossil fuels has motivated the scientific community to seek renewable energy sources as substitutes. Hydrogen is one of the most promising alternative renewable energy sources to replace fossil fuels.[1, 2] Water splitting in general, and electrochemical water splitting in particular, is an effective and environmentally friendly method

to produce hydrogen, and platinum-based materials are the most effective electrocatalyst for the hydrogen evolution reaction (HER). However, the scarcity and high price of Pt limit its wide implementation. Therefore, significant effort has been invested in the search for alternative, Pt-free catalysts that reduce the overpotential and increase energy efficiency compared to the current state of the art. One class of potential candidates are the transition metal dichalcogenide (TMD) family of layered materials (MX_2; M = Mo, W, Nb, Re, etc. and X=S, Se, Te).[1, 3, 4] Among these materials, MoS_2 has drawn particular interest because it offers low cost, a tunable density of exposed electroactive sites along the layer edges, and electrochemical stability in an acidic environment.

The extraordinary physical and chemical properties of layered materials[5-7] has motivated the development of highly controllable synthetic methodologies.[5, 6, 8-14] Hence, TMD isolation can be achieved through chemical exfoliation[5, 11] and their direct growth via chemical vapor deposition (CVD)[13-16] and atomic layer deposition (ALD).[17-21] From the electrocatalytic point of view, chemical approaches for the dispersion of MoS_2 have already demonstrated the assembly of large quantities of these materials on active electrodes. However, the quality and homogeneity of MoS_2 within the dispersion and thus on the final working electrode are difficult to control.[7, 11] The efficiency of the working electrode is governed by the catalyst properties and the conducting support material. Hence, the careful design of the catalyst and its conducting support is of utmost importance. A very convenient approach to fabricate efficient electrodes for electrocatalysis is based on the integration of 2D-TMDs with a highly conductive support material. Large surface areas (3D porous structures) and high electrical conductivity of the active HER electrocatalysts represent two important factors that are key for enhancing and optimizing catalytic activity.[1, 22] The coating of 3D structures such as porous materials using wet chemical approaches can be challenging due to the wetting behavior and diffusion-based limitations within pores having a wide range of sizes, often characteristic of such materials. CVD, as a non-line-of-sight gas phase growth methodology, is considered a very promising method to achieve large-scale and high quality TMD films on porous substrates.[5, 6, 9-11, 15, 16] It can also be used to coat 3D features, but careful tuning of the chamber pressure and temperature is needed to avoid thickness inhomogeneities due to different flow regimes within the 3D porous matrix. ALD, in contrast, enables atomic layer control and conformal deposition using sequential, self-limiting surface reactions,[23, 24] and is a well-established methodology for the deposition of ultra-thin coatings on both flat and 3D substrates.[23, 24] Furthermore, recent developments enable ALD

processes at atmospheric pressure,[25, 26] which increases deposition rates and lowers costs. From the application point of view, 3D porous structures with high surface area are advantageous for electrocatalysis as they can provide higher current densities at lower overpotentials.[27-29] Note that the controlled formation of 3D heterostructures is of crucial importance in many scientific and technological fields. Despite advances in the preparation of porous electrocatalysts,[27, 29-32] the synthesis of such complex 3D heterostructures remains a great challenge, and improved, scalable methodologies are needed for the conformal coating of sub-micron porous materials.

Here we study the deposition of thin MoS_2 layers on 3D foams via ALD and investigate how the degree of crystallinity affects the resulting catalytic performance for the HER. 3D graphene frameworks, having good thermal, mechanical, chemical and electrochemical stability, as well as high electrical conductivity, low density, high surface areas, and tunable pore sizes, proved to be good candidates as support materials for HER electrodes.[1, 22, 27, 29-33] Hence, CVD-derived[10, 33-36] graphene foams (GF) with different pore sizes are used here as the 3D conducting support. Following the synthesis of the GFs with variable pore size, thin MoS_2 layers were deposited as a catalyst using a recently developed ALD process.[17] Although ALD has been used to synthesize conformal MoS_2 coatings on flat substrates,[17, 20, 21] its use to coat TMDs on high-aspect ratio materials is rare.[37, 38] Here we explore two main approaches for the improvement of MoS_2-based electrocatalysts: *i.* control the number and activity of active sites, and *ii.* improve the electron transport between electrode and electrocatalyst for effective proton reduction. The first approach was addressed by controlling the crystallinity of the MoS_2 phase annealed at different temperatures (300-800 °C) while the second was achieved by combining the thin MoS_2 layer and a highly conducting and porous graphene foam. The growth and structure characterization, by means of SEM, TEM, EDX, XPS, and Raman spectroscopy, are described. We conclude by demonstrating the promising catalytic properties and stability of such binder-free 3D heterostructures for the HER. The reported methodology for the formation of the complex 3D TMD/GF could be extended by doping of the MLG (multi-layer graphene) with boron or nitrogen to increase the charge carrier concentration and/or doping the MoS_2 with transition metals during ALD, thus enhancing the catalytic activity even further.

EXPERIMENTAL SECTION

Materials Synthesis

Graphene foam

A commercial Ni foam with an average pore size of 580 μm (INCOFOAMTM, Novamet Specialty Products Corp., 99.999 %) was used as the growth-template. Low-density (LD) foams were prepared using these materials as received.[33] To prepare the high density (HD) foams, a paste was made of Ni powder (3-7 micron, 99.9%, Alfa Aesar) mixed with isopropanol (IPA). This paste was infiltrated into the foams by experimenting with the viscosity and applying manual mechanical pressure, and then allowing to dry in air for 24 h. The growth and Ni etching processes are the same for both materials. For the CVD growth, the Ni foams were cut into 2x4 cm^2 strips, and placed at the center of a 1” fused quartz tube in a hot-wall furnace (TF55035COMC-1, Lindberg® BlueM®). The furnace was heated to 1000 °C (20 °C/min) at atmospheric pressure under flowing Ar (5 sccm, 99.9999 %) and H_2 (20 sccm, 99.9999 %). The system was held at 1000 °C for 30 min to anneal the Ni foam. CH_4 (99.9999 %) was then introduced at a rate of 5 sccm for 60 min at 1000 °C, and finally the furnace was cooled (100 °C min^{-1}) to room temperature. The Ni was then etched in an $FeCl_3$ solution (0.5 M, reagent grade, 97%, Sigma-Aldrich), washed gently with deionized water (DIW), and soaked in a 10M HCl solution (Bio-Lab, 32%) for ~2 hrs. to remove Ni impurities. Finally, the foams were rinsed with IPA and dried on a hot plate in air at 100 °C for 30 min.

Atomic layer deposition of MoS_2

Approximately 10 nm thick MoS_2 layers were grown on the graphene foams by sequential pulsing of H_2S and $Mo(NMe_2)_4$.[17] Growth was performed in a hot-wall viscous-flow reactor (modified Ultratech Savannah S200 with insulated lid) in continuous flow mode at 80 °C. H_2S was supplied at ca. 1 Torr as 5% H_2S in N_2 (Matheson), $Mo(NMe_2)_4$ was supplied at ca. 25 mTorr from a cylinder heated to 80°C, and N_2 (99.999%, Airgas) was used as a carrier gas at a flow rate of 20 sccm. The graphene foams were fixed by carbon tape on a metal substrate and degassed for > 15 min in the reactor prior to growth. Each cycle of MoS_2 growth followed the sequence: 5 s $Mo(NMe_2)_4$ dose, 15 s purge, 1 s H_2S dose, and 15 s purge. The MoS_2 thickness was monitored with an in-situ quartz crystal microbalance (QCM) and confirmed with AFM imaging of step heights on planar test substrates.

Annealing of the ALD-Deposited MoS_2/GFs

The amorphous MoS_2/GFs were placed at the center if a 1” tube furnace. Sulfur powder (500 mg, 99.9% Sigma-Aldrich) was placed upstream and heated separately to ~180 °C using heating tape. An Ar (20 sccm, 99.9999 %) flow was used to flush air from the system and as the carrier

gas. The furnace was then heated to the desired annealing temperature (300-800 °C) and maintained for 20 min. The furnace was then allowed to cool at a rate of ca. 20 °/min.

Materials Characterization

Raman spectroscopy and photoluminescence measurements were carried out in a LabRam HR Evolution system from Horiba Jobin Yvon (λ= 532 nm). Scanning electron microscopy (SEM) analysis was carried in a FEI Quanta 200F ESEM equipped EDS detectors. Transmission electron microscopy (TEM) was carried out directly on the samples grown on samples mechanically exfoliated on lacey carbon coated Cu TEM grids using either JEOL JEM2100 or FEI Tecnai F20-UT TEMs operating at 200 kV. XPS measurements were performed on a Kratos AXIS-Ultra DLD spectrometer, using a monochromatic Al kα source at 75 W and detection pass energies in the range of 20-80 eV. The base pressure in the analysis chamber was $5x10^{-10}$ Torr. Ion sputtering was applied by a 4 kV beam of Ar+ ions, at incidence of 45˚. Due to the structured surface morphology of the samples, very short sputtering steps were initially taken, such as to identify the early incremental changes at domains of direct accessibility by the beam. Gradually longer sputtering steps were then taken in order to identify beam-induced artifacts (to be considered also for the analysis of the initial steps).

Electrochemical Hydrogen Evolution Reaction

Electrochemical measurements were conducted at room temperature in a three-electrode glass cell using a Bio-Logic VSP-300 potentiostat. All the potentials were calibrated to a reversible hydrogen electrode (RHE) and the catalytic activity was compared to platinum. The stability was measured using cyclic voltammetry out to 3000 cycles in an N_2-saturated 0.5 M H_2SO_4 electrolyte with a scan rate of 200 mVs^{-1} and potential region of 0.3 V and -0.3 vs. RHE. Linear sweep voltammetry with a scan rate of 5 mVs^{-1} in potential region from 0.3 V to -0.38 vs RHE was recorded before and after the cycling. The reference electrode was Ag/AgCl (in 3.5 M KCl solution), a graphite rod (Alfa Aesar, 99.9995%) was used as the counter electrode,[39] and a graphite rod electrode attached to different MoS_2/GFs was used as the working electrode.

Electrochemical surface area (ECSA) was measured using the double-layer capacitance method at room temperature. This method is based on double-layer capacitance as measured from voltammetric curves, which were recorded at various scan rates. A plot of the charging current vs. scan rate is constructed. Under the condition where the double layer charging is the only process occurring in that potential range, this plot is a straight line, the slope of which yields the

value of double layer differential capacitance. The surface area can then be calculated by referring the capacitance obtained to the reference value of capacitance per the unit area (C_{ref}): ESA = C/C_{ref}.

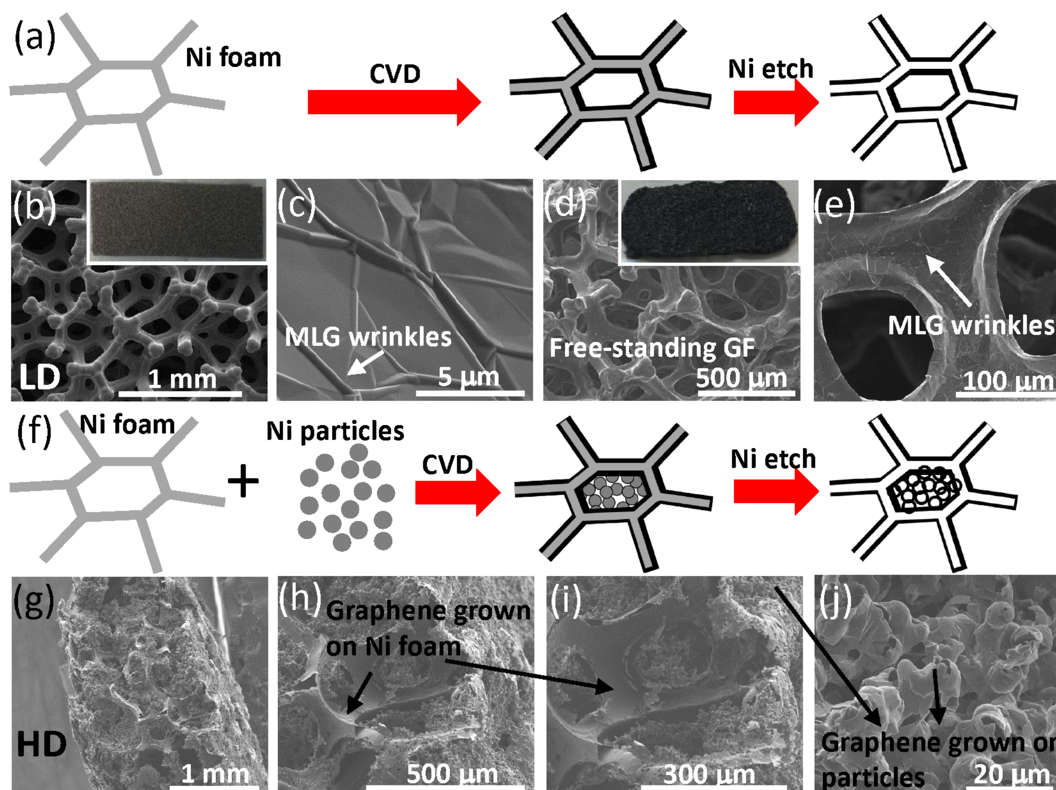

Figure 1: Multi-layer graphene (MLF) foam formation. (a) Schematic representation of the formation of the low-density (LD) foams. (b)-(c) SEM images of low and high magnification of the MLG coated Ni foam. The inset in (b) show an optical image of a ~2.5 cm long G/Ni foam. (d)-(e) SEM images of the same foam after etching of the Ni. The inset in (d) shows an optical image of the Ni-free foam. (f) Schematic representation of assembly of the high-density (HD) foams. (g)-(j) SEM images with increasing magnification of a free-standing HD-GF, showing the graphene grown on the original Ni foam and on the Ni particles.

RESULTS AND DISCUSSION

Graphene Foam Formation

The methodology used here for the synthesis of the two types of graphene foams is illustrated in Figure 1. Low density (LD) GF foam, is obtained using commercial nickel foams as the growth template, and the growth of the multi-layer graphene (MLG) was achieved via CVD, as reported previously.[33] Figure 1 (a) shows a schematic representation of the process, and Figures 1(b)-(e) show SEM images at the different stages. The multilayer coated Ni foam is shown in (b)-(c), where the inset in (b) shows an optical image of the foam at this stage. The stand-alone GF is shown in (d)-(e), and the respective optical image as an inset in (d). Figure S1 shows the Raman

spectra of such graphene foams, suggesting a high quality graphene with AB stacking.[40] In order to reduce the pore size in the above GFs, a powder technology approach was implemented. In this scheme, the commercial Ni foam is first loaded with Ni particles (see Experimental Section) and then MLG is grown by CVD. An annealing step in H_2 prior to the growth (see Experimental Section) sinters the Ni particles to each other and to the original Ni foam, resulting in a complex hierarchical 3D Ni foam template for the subsequent growth of high-density (HD) GF. Figure S2 shows a MLG-coated Ni foam (prior to Ni etching), in which neck formation can be observed. Figure 1 (f) depicts a schematic representation of the process, and SEM images of the stand-alone HD GF ((g)-(j)) show the graphene grown on both the Ni foam and the particles. The electrical and mechanical properties of the LD and HD GFs are shown in Table S1 and Figure S3, exhibiting a highly conductive 3D framework.

MoS_2/GF 3D Heterostructure Formation

Following the synthesis of the highly conductive and robust GFs, and the selective etching of the Ni to leave a freestanding GF, they were coated with a 10 nm layer of MoS_2 using ALD. This was achieved using a recently reported process and implemented here on the LD- and HD-GFs, as described in the Experimental Section. Figure S4 shows the 10 nm layer on a flat SiO_2/Si sample used for thickness calibration together with a quartz crystal microbalance thickness monitor (QCM). The resultant MoS_2 layer was amorphous and a post-growth annealing step under sulfur atmosphere was conducted at various temperatures, 300-800 °C in order to obtain different degrees of crystallinity. Figure 2 shows a schematic representation of the ALD coating and annealing processes. Characterization of the 3D MoS_2/GF heterostuctures is shown in Figure 3.

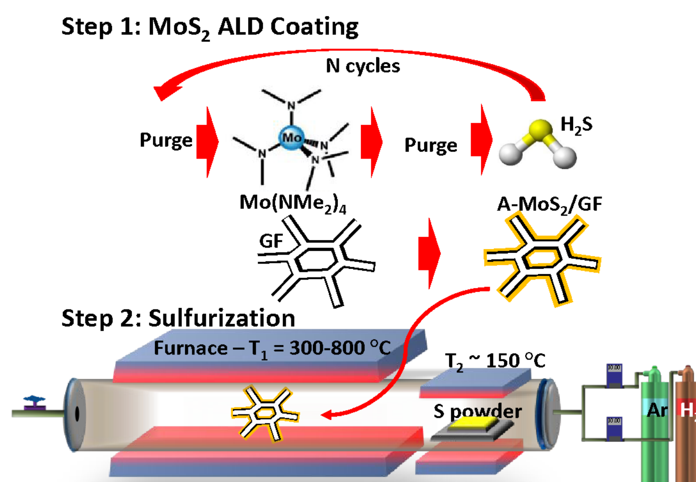

Figure 2: Schematic representation of the MoS_2 ALD coating and the following sulfurization process.

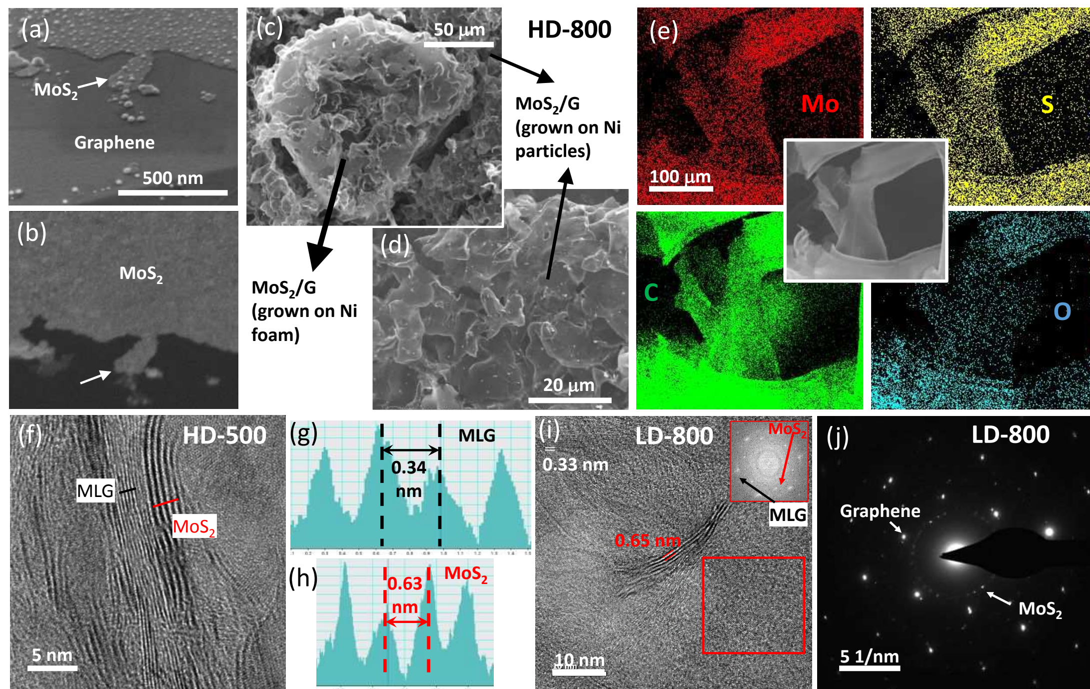

Figure 3: Characterization of the 3D MoS_2/GFs heterostructures: (a)-(b) SEM images taken with different detectors, in-lens (a), and back-scattered electrons (BSE), (b). (c)-(d) SEM images of the HD-800 sample showing that the morphology of the GF is unchanged with the ALD and sulfurization processes. (e) EDS mapping, Mo (red), S (yellow), C (green) and O (light blue) of the area shown in the inset. (f) HRTEM of the HD-500 sample showing the MoS_2 (red) and MLG (black). (g)-(h) analysis of the layer distances in (f). (i) HRTEM of an LD-800 sample showing a standing MoS2 flake or wrinkle in the center. The FFT analysis of the red-square area shows the characteristic peaks for both phases, the MLG and the MoS_2, proving again to have a conformal coating of the GF. (j) Selected area electron diffraction of the same sample in (i), showing the diffraction peaks from both phases.

SEM images from the in-lens and back scattered electrons (BSE) detectors are shown in (a) and (b), respectively. The latter generates contrast based on differences in the atomic mass of the carbon and Mo, so the metal appears much brighter and, thus, is easily distinguished from the graphitic phase. SEM images of the ALD-coated HD foams after sulfurization at 800 °C (Figures 3(c) and (d)) show that the morphology of the HD foam template is preserved. Further SEM images showing the morphology of the 3D high-density GFs before and after etching the Ni, can be seen in Figure S2(f)-(i).

The morphology of the MoS_2 coating was first analyzed on flat samples using AFM, as shown in Figure S4, showing a very smooth film as expected from ALD. Figure S5 shows a series of SEM images, on the as-deposited (a)-(c) and annealed (d)-(e) MoS_2/GFs. It can be clearly seen the formation of some protrusions when annealing at 500 °C. Further annealing to 800 °C exhibit a significant morphological change by the formation of nanocrystallinities and faceted film edges,

mostly planar but occasionally, standing crystals can be observed as well. Important to note, the film continuity is conserved after the annealing.

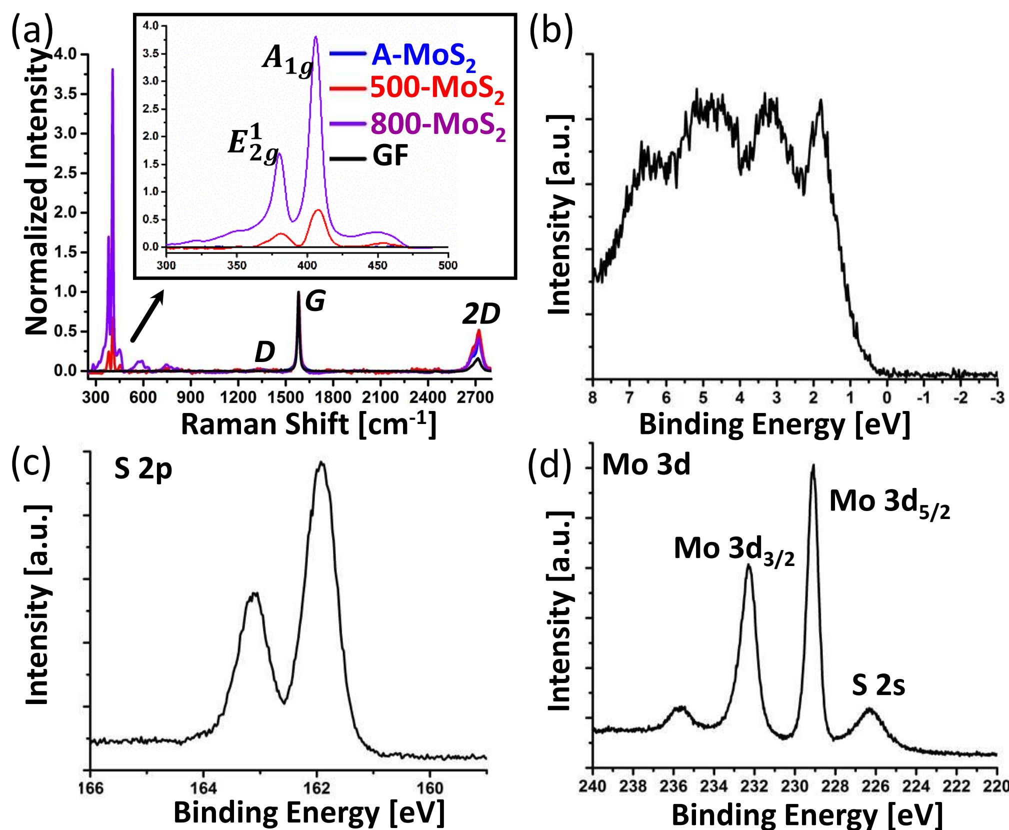

Figure 4: Raman and X-ray photoelectron spectroscopy (XPS) characterization of the 3D heterostructures. (a) Raman spectra showing the normalized (with the G-band of the MLG) characteristic peaks for MoS_2 and MLG for the different samples. The inset is a magnification of the MoS_2 spectra. (b)-(d) XPS windows showing respectively the valence bands, the S 2p and the Mo 3d spectral regions of the LD-800 sample.

In order to evaluate the advantages of using gas-phase methodologies for the production of the 3D MoS_2/GFs, relative to more common wet chemistry approaches, similar 3D heterostructures were made by the deposition of the MoS_2 from solution based on previously reported methods.[30, 31, 41, 42] LD and HD GFs were coated with an ammonium molybdate tetrahydrate solution (as previously reported,[30] see SI), and sulfurized at 800 °C. Figure S6 shows that the wet method changes the HD foam morphology, likely due to capillary effects. We did not observe significant differences in the morphologies of the final 3D heterostructures for LD and HD foams when using ALD-based coatings. This emphasizes the advantages of using gas phase methodologies in general, and ALD in particular, to coat 3D structures: consistency in conformal coating and reproducibility.[24] Further chemical characterization of the ALD-based deposition of MoS_2 on GFs was carried out using energy dispersive spectroscopy (EDS) and mapping of foam

cross-sections. Figure 3(e) shows the EDS mapping for the amorphous-MoS_2 coated GF (as deposited), exhibiting a conformal coating on the 3D foam structure. Further EDS mapping of the annealed samples can be seen in Figure S7. The 3D heterostructured foams were further characterized by transmission electron microscopy (TEM) and selected area electron diffraction (SAED). Figures 3(f) show the presence of MLG (black) and MoS_2 (red) in a HD-500 sample (high-density MoS_2/graphene foam sulfurized at 500 °C). The distance between neighboring layers in both phases is emphasized in (g), MLG, and (h), MoS_2. The in-plane imaging of a MoS_2/GF annealed at 800 °C (LD-800), in which some standing MoS_2 layers or a wrinkle are observed, is shown in (i). An FFT analysis from the red-square area is given in the inset, showing peaks corresponding to the graphitic and MoS_2 phases. SAED further confirms the presence of the two crystalline phases (Fig. 3j). Additional TEM data is provided in Figure S8. The influence of sulfurization temperature on the structure of the MoS_2 layer and the GF was interrogated using Raman spectroscopy (Figures 4a, S9 and Table S2).

The ALD-coated MoS_2/GF is known to be amorphous[17] and, indeed, no Raman signal was detected; similar observations were made with annealing at 300 °C. In both cases, only the graphitic peaks, the characteristic G and 2D modes, were detected. The characteristic MoS_2 modes, E_{2g}^{1} and A_{1g}, could be detected only after annealing at 500 and 800 °C, exhibiting peaks characteristic of the 2H-MoS_2 phase,[43] with no evidence of any other phase (e.g. 1T – MoS_2, metal oxides, etc.). The Raman full-width half-maximum (FWHM) decreases with increasing crystallinity of the material. Therefore, the observed inverse relation with the annealing temperature suggests, as expected, that the MoS_2 crystallinity improves with increasing sulfurization temperature. The sample sulfurized at 500 °C yields FWHM of 14.2 and 12.5 cm^{-1} for E_{2g} and A_{1g}, respectively (Table S2). Sulfurization at 800 °C reduces these values to 9.7 and 9.2 cm^{-1}. Since the ALD deposition for all samples was performed under the same conditions, yielding similar thicknesses (~10 nm), the relative intensity of MoS_2 to graphene peaks can serve as an indication of the TMD layer crystallinity. To reliably compare the relative intensities, spectra were normalized to the G mode intensity of the graphene, Figure 4(a). The I(MoS_2: A_{1g})/I(Graphene: G mode) was found to be 0.68 and 3.32 for the samples annealed at 500 °C and 800 °C, respectively, demonstrating the improved structural order of MoS_2 when sulfurized at higher temperatures (Table S2). The absence of the D peak in the GFs indicates that the ALD process and the annealing in sulfur atmosphere do not damage the graphene lattice.

XPS characterization confirms the presence of high quality MoS_2, however with some surface oxidation (mainly to MoO_3). Figure 4(b) shows the MoS_2 valence bands while Figs. 4(c)-(d) present, respectively, the Mo 3d (including S 2s) and S 2p core levels. The valence bands, (b), consist of five characteristic peaks in the energy range of 0–8 eV,[44] at 1.82, 3.2, two overlapping peaks at ~4.4 and 5.2 and a shoulder at 6.6 eV (with an even smaller shoulder at 8.15 eV). These bands are dominated by the five j-states of Mo 4d electrons and provide a qualitative indicator of the MoS_2 quality. Figure 4(c) shows the S 2p doublet, with the 3/2 peak at 161.92 eV. Figure 4d presents the S 2s and Mo 3d lines at 226.3 eV, 229.1 and 232.2 eV, respectively. Curve fitting of this spectrum reveals a finite amount of oxidized Mo as well, appearing as a doublet at 232.57 and 235.70 eV. For the disulfide components, the measured atomic concentration ratio is Mo:S ~ 1:2 (9.83%/19.69%), suggesting a well preserved MoS_2 stoichiometry. The Mo-O phase (presumably MoO_3) is attributed to surface oxidation estimated to be of ~0.8 nm thickness in average (based on standard photoelectron attenuation considerations for flat substrates, thus the actual oxide thickness might be slightly lower for 3D structures). The survey, O 1s and C 1s spectra are shown in Figure S10. A very mild sputtering step (30s at 1.5 μA sample current, rastered across a 7x5 mm^2 area), was used to identify the top surface components, showing a pronounced decrease in the oxygen and carbon signals: The carbon concentration decreased by 28% of its original concentration and the oxygen by 35%. In addition, the oxidized Mo signal was suppressed by 17% of its pre-sputtering intensity. In contrast, the MoS_2 signals increased and a 'new' small signal of partially reduced Mo, presumably MoS, appeared at 228.45 eV, which is likely a consequence of the different sputtering yields for S and Mo. Figure S10 (b) shows related spectra. It should be stressed that the foam morphology creates 'shadowed' regions for which the sputtering is ineffective. As such, the reduced signals provide only a qualitative indication of the top surface components.

Electrochemical hydrogen evolution reaction (HER)

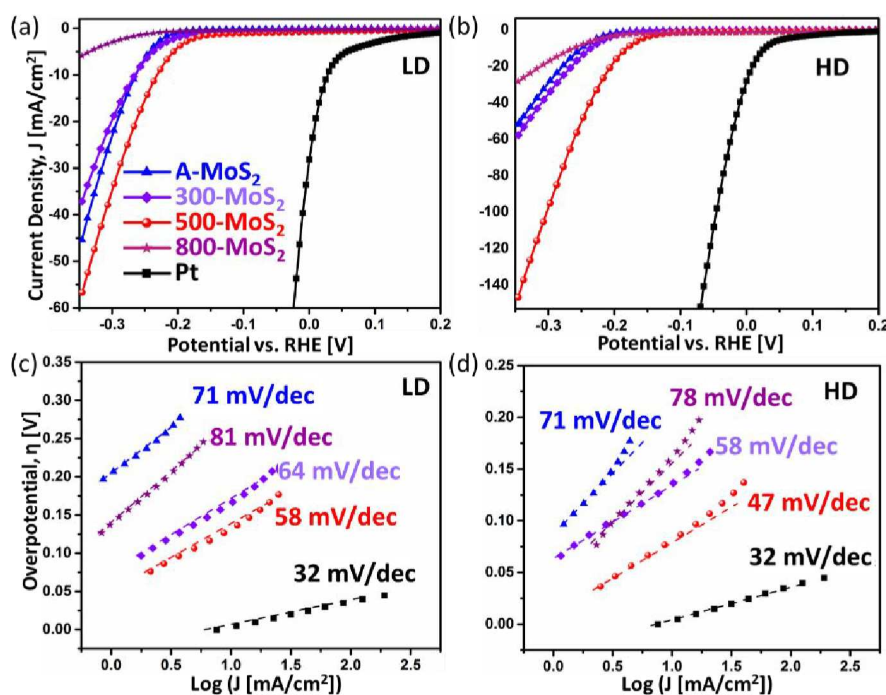

Figure 5 – Hydrogen evolution reaction (HER) measurements: (a) - (b) Polarization curves for the LD and HD samples (with varying °C sulfurization temperature), respectively. (c) - (d) Calculated Tafel slopes for the two types of foams, from the curves

Here we aimed to characterize the electrocatalytic behavior of the two-types of MoS_2/GF 3D heterostructures, the LD and HD foams, as a function of sulfurization temperature. The polarization curves are shown in Figure 5(a) and (b), for the LD and HD foams, respectively. Geometrical surface area was used here in order to allow for comparison between the LD and HD foams. The HER results with a Pt working electrode are shown as a reference (black curve). In both cases, the starting 3D amorphous MoS_2/GF exhibits a good catalytic performance, with overpotentials of 264 and 247mV for the LD and HD foams (at j=-10 mA/cm^2), respectively. Sulfurization at 300 °C has little influence (Figure 5(a)-(b)), suggesting it makes minor structural differences to the MoS_2 phase. Further increase in the sulfurization temperature to 500 °C caused significant improvement in catalytic properties, as seen in the polarization curves, especially for the HD foam. An overpotential as low as 180 mV was obtained for the HD foam sulfurized at 500 °C (HD-500). However, further increase of the sulfurization temperature to 800 °C resulted in a significant decline in catalytic performance, as seen by the large overpotential, (at j = -6 mA/cm^2) that resembles values reported for crystalline MoS_2 (>350 mV).[45]

The Tafel slope is one of the most important metrics in HER evaluation as it represents the voltage increase needed to raise the current by 10x. A lower slope means that the HER kinetics

increase faster with the working potential and therefore, implies a better catalyst.[1] Tafel slopes were extracted from the present polarization curves and are shown in Figures 5(c) and (d) for the LD and HD foams, respectively. It is evident that the Tafel slope decreases on raising the sulfurization temperature to 500 °C, to the lower values of 56 and 47 mV/dec for the LD-500 and HD-500 foams. Further increasing the sulfurization temperature to 800 °C causes an increase in the Tafel slope, reaching the original values of the starting material, the amorphous MoS_2/GFs. The exchange current density is another important parameter related to the inherent activity of the catalyst. Here again, the larger exchange current densities were achieved for the LD- and HD-500. The exchange current density, Tafel slopes and overpotential for the two type of foams as a function of the sulfurization temperature, are summarized in Table 1 and Figures 6(a) - (c).

Table 1: HER Catalytic Performance of the MoS_2/GFs

Sample	*Overpotential, η (@ j=-10 mA/cm^2) [mV]*	*Tafel Slope [mV/dec]*	*Exchange Current, j_0 [μA/cm^2]*
LD-A	264	71	8.4
LD-300	266	64	8.5
LD-500	**231**	**56**	**11**
LD-800	350 (@ j=-6mA/cm^2)	81	9.5
HD-A	247	71	9.6
HD-300	235	58	10.9
HD-500	**180**	**47**	**17.1**
HD-800	261	78	9.6

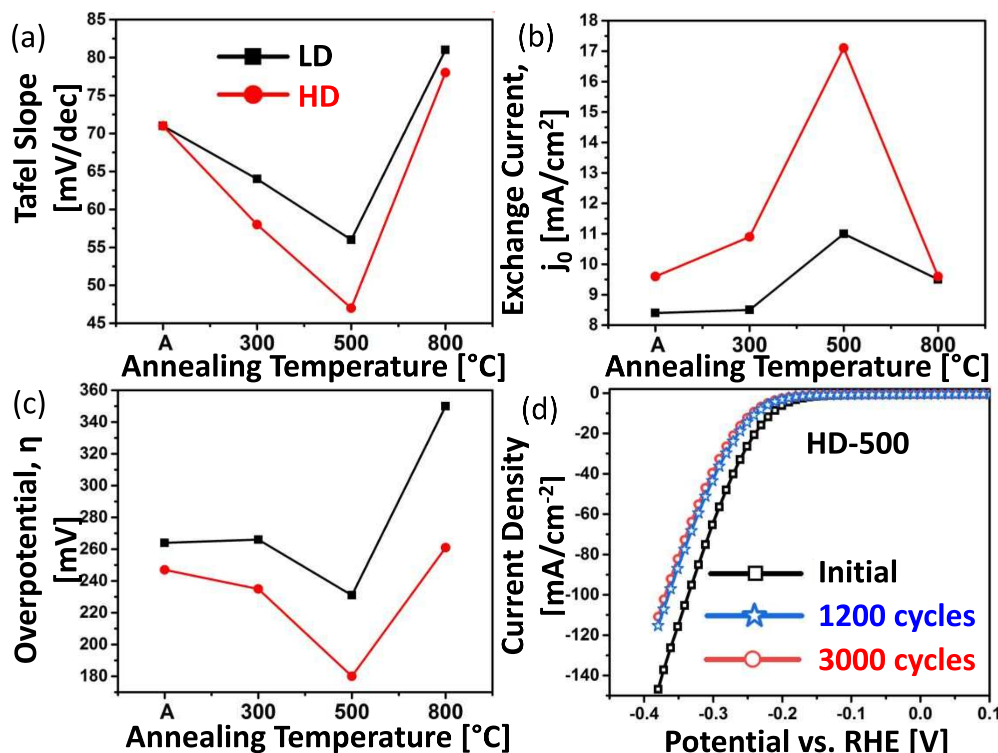

Figure 6 – Annealing temperature effects and catalyst stability: (a) - (c) Tafel slopes, overpotential and exchange currents obtained as a function of sulfurization temperature. (d) Stability test showing the polarization curve for the HD-500 sample at the initial (black), 1200 cycles (blue) and 3000 cycles (red).

The effect of the annealing temperature on the catalytic properties can be visualized from the polarization curves and Tafel slopes, Figures 5 (a)-(d). MoS_2 crystallinity is known to increase with sulfurization temperature,[46, 47] as evident from the Raman data presented in Figure 4(a) and Table S2. The basal plane of the MoS_2 has low catalytic activity and therefore, the reduction in the current density seen in the polarization curves and raising of the Tafel slopes (Figure 5) results from raising the annealing temperature to 800 °C.[45] In contrast, it is well known that defects in the MoS_2 phase, such as edges, vacancies, etc., act as preferred catalytic sites and thus, increase the catalytic HER performance.[45] Hence, the higher catalytic HER performance of the amorphous MoS_2 coated GFs relative to the crystalline samples can be understood as a consequence of the higher density of defects present in the amorphous and 300 °C annealed samples compared to the more crystalline MoS_2 annealed at 800 °C. In contrast to previous reports, in which the MoS_2 catalyst was prepared or annealed at low temperatures, up to ~350 °C,[27, 48-50] a significant improvement in the LD and HD MoS_2/GFs hetersotructure catalytic performance is achieved upon sulfurization at 500 °C. Raman and HRTEM characterization

clearly show the presence of crystalline MoS_2 films, apparently with smaller domains as indicated by the FWHM and relative peak intensities (Figure 3 (a) and Table S2) when comparing to sulfurization at 800 °C. The catalytic performance improvement when annealing at 500 °C indicates there is a trade-off between the density of defects (higher for the amorphous and 300 °C annealed samples) and the crystallinity following the sulfurization at higher temperatures. One possible explanation for this phenomena could be a reduction in the resistivity of the MoS_2 film with the thermal treatment, as shown for vapor phase deposited amorphous films[51] and sulfurized thin Mo films,[47] that compensates for the reduction in the density of catalytic sites (defects).

The major difference between the low- and high-density foams, as evident in the polarization curves, is the current density increase for the HD foams. This is expected due to the increase in surface area and thus, the density of catalytic sites, emphasizing again the advantage of using porous materials as electrocatalysts. To confirm that the surface area has indeed increased, the electrochemical active surface area (ECSA) of the graphene foams (LD and HD) was measured, Figure S11. Indeed, a ~4.8-fold increase was found for the HD-GFs, from 4.33 cm^2 (LD) to 20.86 cm^2 (HD), per geometrical surface area, therefore creating significantly more catalytic sites. Interestingly, the current density increase for the HD foams is not fixed for all sulfurization temperatures, Figures 5(a)-(b), increasing from 1.1x for the A-MoS_2 foams, 1.5 (300), 2.6 (500), reaching a maximum of a 4.7-fold raise to the 800°C samples.

The Tafel slope is an inherent property of the catalyst, and therefore, the same material system, *i.e*. MoS_2/GF, is expected to have similar values. Interestingly, this is not the case here when comparing the low- and high-density foams annealed at the same temperature. The Tafel slopes calculated for the LD- and HD-500 samples are 57 and 47 mV/dec, respectively, therefore showing a ~18 % reduction. The measured overpotential for the same pair of samples (LD- and HD-500) shows a reduction of more than 20%, from 230 mV (LD-500) to 180 mV for the HD-500 sample, and more than 50% increase was obtained for the exchange currents (from 11, for the LD-500, to 17 $\mu A/cm^2$, for the HD-500 foam). A similar trend, but with milder variations, is observed for the remainder of the samples. Therefore, the HD heterostructure foams may have structural and/or chemical differences arising probably from curvature effects of the MoS_2 layers on top of the MLG grown on the Ni particles (comparing to the one grown on the Ni foam). This may lead to an increase in the surface area of the HD-500 sample, strained MoS_2

regions and different grain size and orientations, which may have a high impact on the catalytic sites.[52-54] This may explain also the differences in the current density increase, as mentioned above, for the HD foams annealed at different temperatures. Further work is needed in order to explain the observed catalytic differences between the LD and HD foams and to study the structural and chemical differences between them.

The low Tafel slopes, relatively large exchange current densities and moderate overpotential values suggest that the 3D MoS_2/GFs sulfurized at 500 °C are good candidates as electrocatalysts for the hydrogen evolution reaction. Table 1 summarizes the measured overpotentials, Tafel slopes and exchange currents for all the samples. These results are among the best obtained using 2H-MoS_2 catalysts. For example, the best reported results, to our knowledge, on amorphous and defect-rich MoS_2 thin films exhibit overpotentials around 180-250 mV and Tafel slopes of 40-60 mV/dec.[50, 55, 56] A recent study on sputtered MoS_2 films showed an overpotential of 180 mV and Tafel slope around 45 mV/dec.[57] Despite these promising results, most of the methodologies used have moderate or low ability to coat 3D nanoporous materials. Vapor phase methods relaying on the evaporation of metal oxide precursors (usually MoO_3),[58-60] which is the most common CVD-based procedure for the synthesis of TMD layers,[12-14] have a growth temperature limitation of > ~600 °C, due to the low vapor pressure of the MoO_3 precursor.[12, 14] This limitation inhibits the study of MoS_2 coatings formed at lower temperatures, and based on the present work, achieving improved catalytic performance. Previous reports on ALD-derived MoS_2 films reported higher overpotentials (>220 mV) and Tafel slopes (>47 mV/dec) compared to the present results.[48, 49, 61, 62] As mentioned in the Introduction, many attempts have been made to fabricate MoS_2/graphene (or other carbon) heterostructures to be used as HER electrocatalysts, with and without metal supports. The vast majority used wet-chemical approaches, therefore having moderate compatibility with nanoporous support materials. The electrocatalytic results in those cases span a wide, 42-54 mV/dec range of Tafel slopes, and 140-350 mV overpotentials.[27, 30-32, 58, 59, 63] Table S3 summarizes the comparisons above, arguing the results reported herein are among the best for 2H-MoS_2-based catalysts with improved compatibility with 3D porous support materials, as required for practical applications.

Stability tests were conducted by cycling the measurements 3000 times. Figure 6 (d) shows the polarization curves for the best sample, the HD-500, at the initial (black), 1200 cycles (blue) and

3000 cycles (red). Similar curves for the rest of the samples are shown in Figure S12. Despite their low catalytic performance, the better stability and thus smaller change in the overpotential and Tafel slopes between the initial cycle and after 3000 cycles, were achieved for the higher sulfurization temperature samples, the LD- and HD-800, likely due to their higher crystallinity. This is followed by the LD- and HD-500 samples, which exhibit the best catalytic performance with overpotentials as low as 231 and 180 mV, and Tafel slopes of 56 and 47 mV/dec. The amorphous and 300 °C sulfurized samples exhibit good catalytic performance, lower than the 500 °C samples, with lower stability, Figure S12. The overpotential and Tafel slopes derived for all the samples at the initial stage and after 3000 cycles are shown in Figure S12 (d).

CONCLUSIONS

In summary, we demonstrated the use of ALD as an effective process for conformal MoS_2 coatings of MLG foams of different pore sizes. The crystallinity of the MoS_2 coating is tunable via the sulfurization temperature, with a significant effect on the catalytic performance and a maximum efficiency at 500 °C, as tested. Although amorphous MoS_2 is considered to be a very good catalyst, when high density of defects/catalytic sites are present, we find that there is a trade-off between the density of such sites and the crystallinity of the sample. Exploiting this trade-off, one can optimize the catalytic and charge transport properties with respect to the MoS_2 crystallinity density of grain boundaries), crystal orientation and strain that may be related to the MoS_2/GFs heterostructure morphology. Our findings are competitive with the best results reported so far with the intrinsic 2H-MoS_2 phase. We have demonstrated high exchange currents (17 μA/cm^2), very low Tafel slopes (47 mV/dec) and moderate overpotentials (180 mV), making our approach a good platform for the design of binder-free, light-weight and complex 3D electrocatalysts. Moreover, this approach could potentially be further improved by doping the GF support material to increase the charge carrier density, or by doping the MoS_2 layer to increase its catalytic activity.

Acknowledgements

J.T. acknowledges the generous support from MAFAT, grant # 0605814213, R.D. is grateful to the Israel Science Foundation, project # 1784/15. E.H., B.A.R. and A.I. gratefully acknowledge the support from the Israel Science Foundation, grant # 2171/17. This research was supported by

the Materials Research Science and Engineering Center (MRSEC) of Northwestern University (NSF DMR-1720139) and the 2-DARE program (NSF EFRI-1433510). A.H. acknowledges the support of a Research Fellowship from the Deutsche Forschungsgemeinschaft (grant HE 7999/1-1). M.J.M. gratefully acknowledges support via a 3M Fellowship, as well as from the Ryan Fellowship and the Northwestern University International Institute for Nanotechnology. This work made use of the Northwestern University NUANCE Center, which are partially supported by the Soft and Hybrid Nanotechnology Experimental (SHyNE) Resource (NSF ECCS-1542205), the Materials Research Science and Engineering Center (NSF DMR-1720139), the state of Illinois, and Northwestern University.

REFERENCES

1. M. Zeng and Y. Li, *Journal of Materials Chemistry A*, 2015, **3**, 14942-14962.
2. J. A. Turner, *Science*, 2004, **305**, 972-974.
3. S. Chandrasekaran, L. Yao, L. Deng, C. Bowen, Y. Zhang, S. Chen, Z. Lin, F. Peng and P. Zhang, *Chem. Soc. Rev.*, 2019, **48**, 4178-4280.
4. H. Jin, C. Guo, X. Liu, J. Liu, A. Vasileff, Y. Jiao, Y. Zheng and S.-Z. Qiao, *Chem. Rev.*, 2018, **118**, 6337-6408.
5. S. Z. Butler, S. M. Hollen, L. Cao, Y. Cui, J. A. Gupta, H. R. Gutierrez, T. F. Heinz, S. S. Hong, J. Huang, A. F. Ismach, E. Johnston-Halperin, M. Kuno, V. V. Plashnitsa, R. D. Robinson, R. S. Ruoff, S. Salahuddin, J. Shan, L. Shi, M. G. Spencer, M. Terrones, W. Windl and J. E. Goldberger, *Acs Nano*, 2013, **7**, 2898-2926.
6. G. Fiori, F. Bonaccorso, G. Iannaccone, T. Palacios, D. Neumaier, A. Seabaugh, S. K. Banerjee and L. Colombo, *Nature Nanotechnology*, 2014, **9**, 768-779.
7. K. S. Novoselov, V. I. Fal'ko, L. Colombo, P. R. Gellert, M. G. Schwab and K. Kim, *Nature*, 2012, **490**, 192-200.
8. A. Ismach, H. Chou, P. Mende, A. Dolocan, R. Addou, S. Aloni, R. Wallace, R. Feenstra, R. S. Ruoff and L. Colombo, *2d Materials*, 2017, **4**.
9. A. Ismach, C. Druzgalski, S. Penwell, A. Schwartzberg, M. Zheng, A. Javey, J. Bokor and Y. Zhang, *Nano Lett.*, 2010, **10**, 1542-1548.
10. X. Li, W. Cai, J. An, S. Kim, J. Nah, D. Yang, R. Piner, A. Velamakanni, I. Jung, E. Tutuc, S. K. Banerjee, L. Colombo and R. S. Ruoff, *Science*, 2009, **324**, 1312-1314.
11. F. Bonaccorso, A. Lombardo, T. Hasan, Z. P. Sun, L. Colombo and A. C. Ferrari, *Mater. Today*, 2012, **15**, 564-589.
12. O. Hod, M. Urbakh, D. Naveh, M. Bar-Sadan and A. Ismach, *Adv. Mater.*, 2018, **30**.
13. Y. Liu, R. Ghosh, D. Wu, A. Ismach, R. Ruoff and K. Lai, *Nano Lett.*, 2014, **14**, 4682-4686.
14. G. Radovsky, T. Shalev and A. Ismach, *Journal of Materials Science*, 2019, **54**, 7768-7779.
15. Z. Y. Cai, B. L. Liu, X. L. Zou and H. M. Cheng, *Chem. Rev.*, 2018, **118**, 6091-6133.
16. Y.-H. Lee, X.-Q. Zhang, W. Zhang, M.-T. Chang, C.-T. Lin, K.-D. Chang, Y.-C. Yu, J. T.-W. Wang, C.-S. Chang, L.-J. Li and T.-W. Lin, *Adv. Mater.*, 2012, **24**, 2320-2325.
17. T. Jurca, M. J. Moody, A. Henning, J. D. Emery, B. H. Wang, J. M. Tan, T. L. Lohr, L. J. Lauhon and T. J. Marks, *Angewandte Chemie-International Edition*, 2017, **56**, 4991-4995.

18. M. J. Moody, A. Henning, T. Jurca, J. Y. Shang, H. Bergeron, I. Balla, J. N. Olding, E. A. Weiss, M. C. Hersam, T. L. Lohr, T. J. Marks and L. J. Lauhon, *Chem. Mater.*, 2018, **30**, 3628-3632.
19. Z. Jin, S. Shin, D. H. Kwon, S. J. Han and Y. S. Min, *Nanoscale*, 2014, **6**, 14453-14458.
20. J. J. Pyeon, S. H. Kim, D. S. Jeong, S. H. Baek, C. Y. Kang, J. S. Kim and S. K. Kim, *Nanoscale*, 2016, **8**, 10792-10798.
21. L. K. Tan, B. Liu, J. H. Teng, S. F. Guo, H. Y. Low and K. P. Loh, *Nanoscale*, 2014, **6**, 10584-10588.
22. G. Zhao, K. Rui, S. X. Dou and W. Sun, *Adv. Funct. Mater.*, 2018, **28**.
23. N. P. Dasgupta, X. Meng, J. W. Elam and A. B. F. Martinson, *Acc. Chem. Res.*, 2015, **48**, 341-348.
24. S. M. George, *Chem. Rev.*, 2010, **110**, 111-131.
25. R. L. Z. Hoye, D. Munoz-Rojas, S. F. Nelson, A. Illiberi, P. Poodt, F. Roozeboom and J. L. MacManus-Driscoll, *Apl Materials*, 2015, **3**.
26. D. Muñoz-Rojas and J. MacManus-Driscoll, *Materials Horizons*, 2014, **1**, 314-320.
27. Y.-H. Chang, C.-T. Lin, T.-Y. Chen, C.-L. Hsu, Y.-H. Lee, W. Zhang, K.-H. Wei and L.-J. Li, *Adv. Mater.*, 2013, **25**, 756-760.
28. S. R. Kadam, U. V. Kawade, R. Bar-Ziv, S. W. Gosavi, M. Bar-Sadan and B. B. Kale, *ACS Applied Energy Materials*, 2019, **2**, 5900-5908.
29. Q. Yun, Q. Lu, X. Zhang, C. Tan and H. Zhang, *Angewandte Chemie-International Edition*, 2018, **57**, 626-646.
30. P. Zhu, Y. Chen, Y. Zhou, Z. Yang, D. Wu, X. Xiong and F. Ouyang, *Int. J. Hydrogen Energy*, 2018, **43**, 14087-14095.
31. Y. Yan, B. Xia, N. Li, Z. Xu, A. Fisher and X. Wang, *Journal of Materials Chemistry A*, 2015, **3**, 131-135.
32. Z. Pu, Q. Liu, A. M. Asiri, A. Y. Obaid and X. Sun, *J. Power Sources*, 2014, **263**, 181-185.
33. Z. Chen, W. Ren, L. Gao, B. Liu, S. Pei and H.-M. Cheng, *Nature Materials*, 2011, **10**, 424.
34. R. Piner, H. Li, X. Kong, L. Tao, I. N. Kholmanov, H. Ji, W. H. Lee, J. W. Suk, J. Ye, Y. Hao, S. Chen, C. W. Magnuson, A. F. Ismach, D. Akinwande and R. S. Ruoff, *Acs Nano*, 2013, **7**, 7495-7499.
35. L. Ji, H. Zheng, A. Ismach, Z. Tan, S. Xun, E. Lin, V. Battaglia, V. Srinivasan and Y. Zhang, *Nano Energy*, 2012, **1**, 164-171.
36. L. Zhang, D. DeArmond, N. T. Alvarez, D. Zhao, T. Wang, G. Hou, R. Malik, W. R. Heineman and V. Shanov, *Journal of Materials Chemistry A*, 2016, **4**, 1876-1886.
37. D. K. Nandi, S. Sahoo, S. Sinha, S. Yeo, H. Kim, R. N. Bulakhe, J. Heo, J. J. Shim and S. H. Kim, *Acs Applied Materials & Interfaces*, 2017, **9**, 40252-40264.
38. D. H. Xiong, Q. Q. Zhang, W. Li, J. J. Li, X. L. Fu, M. F. Cerqueira, P. Alpuim and L. F. Liu, *Nanoscale*, 2017, **9**, 2711-2717.
39. R. J. Wei, M. Fang, G. F. Dong and J. C. Ho, *Science Bulletin*, 2017, **62**, 971-973.
40. L. M. Malard, M. A. Pimenta, G. Dresselhaus and M. S. Dresselhaus, *Physics Reports-Review Section of Physics Letters*, 2009, **473**, 51-87.
41. J. Xie, J. Zhang, S. Li, F. Grote, X. Zhang, H. Zhang, R. Wang, Y. Lei, B. Pan and Y. Xie, *J. Am. Chem. Soc.*, 2013, **135**, 17881-17888.
42. B. T. Liu, S. W. Wang, Q. H. Mo, L. L. Peng, S. X. Cao, J. Wang, C. R. Wu, C. Li, J. Guo, B. Q. Liu, W. B. Chen and Y. Lin, *Electrochim. Acta*, 2018, **292**, 407-418.
43. S. J. Sandoval, D. Yang, R. F. Frindt and J. C. Irwin, *Physical Review B*, 1991, **44**, 3955-3962.

44. K. S. Liang, G. J. Hughes and R. R. Chianelli, *Journal of Vacuum Science & Technology a-Vacuum Surfaces and Films*, 1984, **2**, 991-994.
45. T. F. Jaramillo, K. P. Jorgensen, J. Bonde, J. H. Nielsen, S. Horch and I. Chorkendorff, *Science*, 2007, **317**, 100-102.
46. H. Hadouda, J. Pouzet, J. C. Bernede and A. Barreau, *Mater. Chem. Phys.*, 1995, **42**, 291-297.
47. T.-K. Oh, H. Ju, H. Jeon and J.-K. Lee, *Appl. Phys. Lett.*, 2016, **109**, 242104.
48. T. A. Ho, C. Bae, S. Lee, M. Kim, J. M. Montero-Moreno, J. H. Park and H. Shin, *Chem. Mater.*, 2017, **29**, 7604-7614.
49. D. H. Kwon, Z. Jin, S. Shin, W.-S. Lee and Y.-S. Min, *Nanoscale*, 2016, **8**, 7180-7188.
50. J. F. Xie, H. Zhang, S. Li, R. X. Wang, X. Sun, M. Zhou, J. F. Zhou, X. W. Lou and Y. Xie, *Adv. Mater.*, 2013, **25**, 5807-+.
51. D. N. Kouvatsos, G. Papadimitropoulos, T. Spiliotis, M. Vasilopoulou, D. Barreca, A. Gasparotto and D. Davazoglou, in *Physica Status Solidi C: Current Topics in Solid State Physics, Vol 12, No 7*, eds. P. Hoffmann, M. Knez, C. Vahlas and S. Alexandrov, 2015, vol. 12, pp. 975-979.
52. D. Liang, Y.-W. Zhang, P. Lu and Z. G. Yu, *Nanoscale*, 2019, DOI: 10.1039/C9NR06541E.
53. B. You, M. T. Tang, C. Tsai, F. Abild-Pedersen, X. L. Zheng and H. Li, *Adv. Mater.*, 2019, **31**.
54. H. Li, C. Tsai, A. L. Koh, L. Cai, A. W. Contryman, A. H. Fragapane, J. Zhao, H. S. Han, H. C. Manoharan, F. Abild-Pedersen, J. K. Norskov and X. Zheng, *Nature Materials*, 2016, **15**, 48-+.
55. D. Merki, S. Fierro, H. Vrubel and X. Hu, *Chemical Science*, 2011, **2**, 1262-1267.
56. B. Li, L. Jiang, X. Li, Z. Cheng, P. Ran, P. Zuo, L. Qu, J. Zhang and Y. Lu, *Adv. Funct. Mater.*, 2019, **29**.
57. F. Xi, P. Bogdanoff, K. Harbauer, P. Plate, C. Hoelm, J. Rappich, B. Wang, X. Han, R. van de Krol and S. Fiechter, *Acs Catalysis*, 2019, **9**, 2368-2380.
58. P. Gnanasekar, D. Periyanagounder and J. Kulandaivel, *Nanoscale*, 2019, **11**, 2439-2446.
59. G. R. Bhimanapati, T. Hankins, Y. Lei, R. A. Vilá, I. Fuller, M. Terrones and J. A. Robinson, *ACS Applied Materials & Interfaces*, 2016, **8**, 22190-22195.
60. H. Wang, Z. Lu, S. Xu, D. Kong, J. J. Cha, G. Zheng, P.-C. Hsu, K. Yan, D. Bradshaw, F. B. Prinz and Y. Cui, *Proceedings of the National Academy of Sciences*, 2013, **110**, 19701-19706.
61. S. Shin, Z. Jin, D. H. Kwon, R. Bose and Y.-S. Min, *Langmuir*, 2015, **31**, 1196-1202.
62. A. Sharma, M. A. Verheijen, L. Wu, S. Karwal, V. Vandalon, H. C. M. Knoops, R. S. Sundaram, J. P. Hofmann, W. M. M. Kessels and A. A. Bol, *Nanoscale*, 2018, **10**, 8615-8627.
63. X. Meng, L. Yu, C. Ma, B. Nan, R. Si, Y. Tu, J. Deng, D. Deng and X. Bao, *Nano Energy*, 2019, **61**, 611-616.

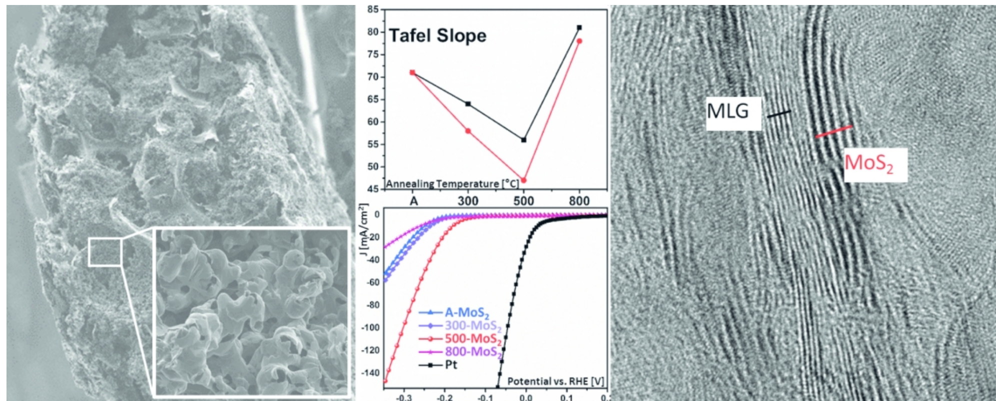
Tafel Slope
Annealing Temperature [°C]
A
300
500
800
J [mA/cm2]
A-MoS2
300-MoS2
500-MoS2
800-MoS2
Pt
Potential vs. RHE [V]
MLG
MoS2